Programming bistability in geometrically perturbed mechanical metamaterials

Yingchao Peng,[1,‡] Imtiar Niloy,[2,‡] Megan Kam,[2] Paolo Celli,[2,*] and Paul Plucinsky[1,†]

[1] *Viterbi School of Engineering, University of Southern California, Los Angeles, California 90089, USA*

[2] *Department of Civil Engineering, Stony Brook University, New York, New York 11794, USA*

(Received 4 March 2024; revised 10 June 2024; accepted 12 July 2024; published 29 July 2024)

Mechanical metamaterials capable of large deformations are an emerging platform for functional devices and structures across scales. Bistable designs are particularly attractive since they endow a single object with two configurations that display distinct shapes, properties, and functionalities. We propose a strategy that takes a common (nonbistable) metamaterial design and transforms it into a bistable one; specifically, by allowing for irregular patterns through geometric perturbations of the unit cell and by leveraging the intercell constraints inherent to the large-deformation response of metamaterials. We exemplify this strategy by producing a design framework for bistable planar kirigami metamaterials, starting from the canonical rotating-squares pattern. The framework comprises explicit design formulas for cell-based kirigami with unprecedented control over the shape of the two stable states and an optimization methodology that allows for efficient tailoring of the geometric features of the designs to achieve target elastic properties as well as shape change. The versatility of this framework is illustrated through a wide variety of examples, including nonperiodic designs that achieve two arbitrarily shaped stable states. Quantitative and qualitative experiments, featuring prototypes with distinct engineering design details, complement the theory and shine light on the strengths and limitations of our design approach. These results show how to design bistable metamaterials from nonbistable templates, paving the way for further discovery of bistable systems and structures that are not simply arrangements of known bistable units.

DOI: 10.1103/PhysRevApplied.22.014073

I. INTRODUCTION

The past few decades have ushered in a paradigm shift in the way in which structural instabilities are perceived: once something to avoid, researchers now design mechanical systems and structures to reversibly buckle as part of their functionality [1–3]. Bistable systems, possessing two morphologically distinct stable states, are pervasive in nature and attractive in engineering. They are key to how a Venus flytrap collects its prey [4] and a beetle unfurls its wings [5] and are leveraged in deployable space structures [6], soft robots [7–9], MEMS devices [10,11], and the like. They are even the cornerstone to popular everyday objects such as PopSockets phone holders and toys such as PopIt fidgets and jumping poppers [12,13].

Bistability comes in a variety of modalities. It is achieved by purely geometric means through tailoring the design of thin-wall structures, such as arches and shells [14], or by designing clever ensembles of structural elements connected by pins or flexural joints [15]. It also emerges through a combination of geometry and material-induced rigidity, as in the case of bistable shells made of composite materials [16], or through prestress, as when multistable shells are obtained from prestretched strips [17]. Bistability can even be facilitated by nuanced features in origami and kirigami, including hinges with limited motion range [18,19] and creases with directional bias [20,21].

Here, we focus on purely geometrical routes to bistability, since design principles in this setting are broadly applicable to a variety of scales, materials, and manufacturing methods. The archetype of a purely geometrical bistable structure is the von Mises truss [22], featuring two inclined elastic bars connected at a hinge and constrained by pin supports. When this structure is loaded at its apex, the bars compress and eventually snap into an inverted tent shape, a second stable state by symmetry. This basic principle leads to a wealth of bistable systems. Cleverly arranged von Mises trusses form the basis for bistable planar lattices [23] and kirigami [15]. Other complex multistable systems arise by exploiting snapping arches and domes [24–31], or more sophisticated bistable units such as the square-twist origami cell [32]. The underlying philosophy to all these works is the same: the key designer input to a complex bistable system is a bistable building block.

*Contact author: paolo.celli@stonybrook.edu

†Contact author: plucinsk@usc.edu

‡These authors contributed equally to this work.

Our work seeks to break away from this prevailing philosophy. Toward this goal, it is notable that many motifs found in origami are bistable even though their basic building blocks are floppy. Examples include Kresling, Waterbomb, and helical tubes [33–35], hypar [36], and the typical origami flasher [37,38]. However, as is often the case with origami, most of these examples have artistic origins and their bistability is serendipitous. The question of what makes them, or any "pattern," bistable remains largely unexplored.

Our objective is to highlight the role of *geometric perturbations* as a fundamental ingredient for bistability and to show that such perturbations, when suitably applied to fairly generic families of patterns, can be used as a versatile platform to design bistable metamaterials with a wide range of target properties. In Fig. 1, we illustrate the key ideas applied to a prototypical two-dimensional (2D) morphing metamaterial called the rotating-squares pattern [39,40]. A single unit cell of this pattern [Fig. 1(a)] is capable of changing its shape through a mechanism [41] or floppy mode [42] given by counter-rotating its panels about the central slit. Symmetry, in turn, makes the intercell constraints redundant: periodic tiling of the cell [Fig. 1(b)] yields a pattern that exhibits the same such mechanism. Breaking the design symmetry, however, reveals an interesting dichotomy: the cell continues to possess a floppy mode [Fig. 1(c)] but the overall pattern does not [Fig. 1(d)]. The intercell constraints are generically no longer redundant. Our main insight is that while generic perturbations yield monostable patterns, careful geometric tuning of these perturbations can turn mechanism-based designs into bistable ones [Fig. 1(d)].

There has been a thrust in recent years to go beyond metamaterials made of canonical unit cells and provide optimization tools to explore the geometry-property relationships in these systems. Singh and van Hecke [43] and Deng *et al.* [44] show that optimizing the geometric features of perturbed rotating-squares designs can yield a rich range of target elastic properties. Mahadevan and colleagues [45,46] use global optimization frameworks to produce nonperiodic generalizations of well-known origami and kirigami metamaterials with target shapes. Hard-encoding design rules in a metamaterial (e.g., for the panels to rotate about flexible hinges or folds), as in Refs. [47–51], yield marching algorithms that improve the optimization schemes, enabling further demonstrations of programmability.

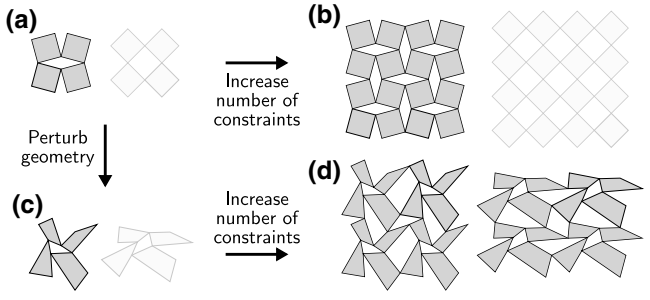

FIG. 1. A geometrical route to bistability. (a) A rotating-squares unit cell, with its mechanism motion shaded in light gray. (b) A periodic and overconstrained version of (a). (c) A perturbed version of (a). (d) A bistable structure obtained by tiling perturbed unit cells, in its first and second stable states.

Our work builds on these ideas under the lens of bistability and with particular emphasis on practical (reduced-order) design tools that can guide experiments at the conceptual or prototyping phase of design. We start by showing how to hard encode bistability in a large class of 2D periodic metamaterials composed of repeating unit cells of panels and slits, termed *planar kirigami* herein and elsewhere [45,52,53], as opposed to kirigami that relies on out-of-plane buckling [54,55]. We then introduce an optimization framework for bistable planar kirigami that incorporates a reduced-order model for the elastic energy, allowing us to tune the designs to achieve target morphing and elastic properties. A suite of representative examples and corresponding experiments follows. We explore examples ranging from classical monolithic planar kirigami configurations to pin-jointed panel systems and truss-based analogues to test the applicability of our design and optimization strategies in a variety of settings. In each case, the experiments validate the bistable behavior of the patterns and certain qualitative features of their elastic properties, but also highlight how our theory can guide but not fully replace high-fidelity models and prototyping. Finally, we showcase the versatility of our design approach by extending it to nonperiodic systems with complex shape change.

II. DESIGN FORMULAS FOR BISTABLE PLANAR KIRIGAMI

We begin by developing a general recipe for bistable planar kirigami comprised of a repeating unit cell of four quad panels and four quad slits, obtained through geometric perturbations of the rotating squares. The recipe amounts to a compact design formula for bistability, which we explain using Fig. 2 as a guide. In Fig. 2(a), we show a generic unit cell representing the first stable state of a quad kirigami design, with the panels and slits labeled by 2D vectors $\mathbf{s}_i$, $\mathbf{t}_i$, $\mathbf{u}_i$, and $\mathbf{v}_i$, $i = 1, \ldots, 4$. In Fig. 2(b), we illustrate its periodicity using the 2D Bravais-lattice vectors $\boldsymbol{\ell}_1^R$ and $\boldsymbol{\ell}_2^R$. In Fig. 2(c), we show the unit cell of the second stable state. Each panel in the cell is rotated in the plane by a right-hand rotation $\mathbf{R}(\phi_i)$ of angle ϕ_i, as shown, taking the initial cell vectors to deformed ones by the transformations $\mathbf{s}_i \mapsto \mathbf{R}(\phi_i)\mathbf{s}_i$, $\mathbf{t}_i \mapsto \mathbf{R}(\phi_i)\mathbf{t}_i$, $\mathbf{u}_i \mapsto \mathbf{R}(\phi_i)\mathbf{u}_i$, and $\mathbf{v}_i \mapsto \mathbf{R}(\phi_i)\mathbf{v}_i$, $i = 1, \ldots, 4$. Finally, in Fig. 2(d), we show

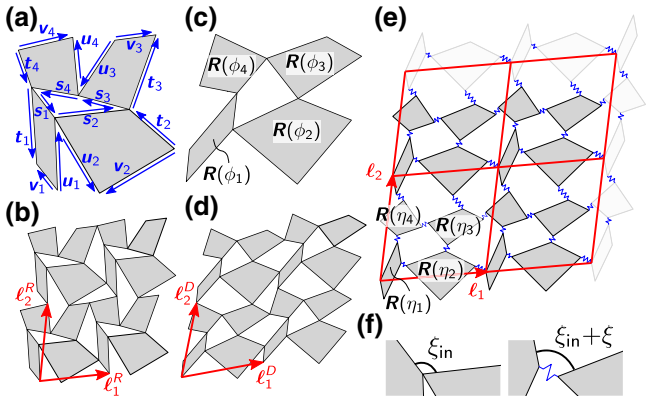

FIG. 2. Perturbed rotating-squares kirigami and the design recipe. (a) The unit cell in its first stable state, indicating the design vectors. (b) The periodicity constraint. (c),(d) The second stable states of (a) and (b), respectively, obtained by rotating each panel by an angle ϕ_i. (e) The elastic energy model. From (b), each panel is rotated and translated periodically to produce a homogeneous effective deformation with Bravais-lattice vectors $\boldsymbol{\ell}_1$ and $\boldsymbol{\ell}_2$. As illustrated, the stored energy is calculated assuming linear springs between the separated panels. (f) Details of the two bottom-left panels of (b) and (e), indicating a change in opening angle.

2D Bravais-lattice vectors $\boldsymbol{\ell}_1^D$ and $\boldsymbol{\ell}_2^D$, quantifying the periodicity in the second stable state. All of these vectors and rotation angles are subject to a variety of constraints for a compatible design, including equality constraints that enforce periodicity and ensure the vectors form closed loops about each panel and slit, as well as inequality constraints that ensure that the panels are convex quadrilaterals that do not overlap. We enumerate all the compatibility conditions in Sec. S1.A of the Supplemental Material [56] and manipulate them into forms broadly useful for design in Secs. S1.B and S1.C of the Supplemental Material [56].

The key result is a design formula that parametrizes all the equality constraints. It takes the form

$$\begin{bmatrix} \mathbf{s}_3 \\ \mathbf{s}_4 \\ \mathbf{t} \\ \mathbf{u} \\ \mathbf{v} \end{bmatrix} = \mathbf{D}(\boldsymbol{\phi}) \begin{bmatrix} \mathbf{s}_1 \\ \mathbf{s}_2 \\ \boldsymbol{\ell} \end{bmatrix}, \tag{1}$$

where $\mathbf{t}, \mathbf{u}$, and $\mathbf{v}$ stack the corresponding $\mathbf{t}_i, \mathbf{u}_i$, and $\mathbf{v}_i$ design vectors into eight component arrays and $\boldsymbol{\ell}$ does likewise for the four Bravais-lattice vectors $\boldsymbol{\ell}_1^R, \ldots, \boldsymbol{\ell}_2^D$. The 28×12 matrix $\mathbf{D}(\boldsymbol{\phi})$, concretely linking these arrays, is a lengthy nonlinear expression of the rotation angles $\boldsymbol{\phi} = (\phi_1, \ldots, \phi_4)$. Its explicit formula is provided in Eq. (S21) in Sec. S1.B of the Supplemental Material [56].

Equation (1) organizes a wealth of information for designing and tuning bistable kirigami structures. The right-hand side contains the designer inputs. It includes the Bravais-lattice vectors, which are the natural descriptors for the target maximum stretch, the Poisson ratio, and the shearing between the two stable states. It also contains eight additional degrees of freedom (DOFs) through the four rotation angles $\boldsymbol{\phi}$ and design vectors $\mathbf{s}_1$ and $\mathbf{s}_2$. Each can be tuned to achieve, for instance, a desirable energy barrier between the two stable states. The remaining parameters describing the designs in Fig. 2 are all stacked on the left-hand side of Eq. (1) and thus are fully determined from these designer inputs.

III. OPTIMIZATION FRAMEWORK FOR ELASTIC TUNING

An appealing aspect to this characterization is that it marries naturally with standard optimization tools to furnish a versatile design framework for tuning bistability. Assume that a designer has in mind two stable states, obtained by prescribing the Bravais-lattice vectors in the reference $\boldsymbol{\ell}_1^R, \boldsymbol{\ell}_2^R$ and deformed $\boldsymbol{\ell}_1^D, \boldsymbol{\ell}_2^D$ configurations. Since there are eight additional parameters on the right-hand side of Eq. (1), the design can be optimized to achieve any general objective that can be written as a minimization problem:

$$\min \left\{ f_{\text{obj}}(\mathbf{s}_1, \mathbf{s}_2, \boldsymbol{\phi}) \;\middle|\; \mathbf{g}_{\text{ineq}}(\mathbf{s}_1, \mathbf{s}_2, \boldsymbol{\phi}) \geq 0 \right\}. \tag{2}$$

In this formulation, $\mathbf{g}_{\text{ineq}}(\mathbf{s}_1, \mathbf{s}_2, \boldsymbol{\phi})$ lists all the inequality constraints that are necessary and sufficient for the pattern to have convex panels and slits in its reference and deformed stable states. These constraints, which are written out explicitly in the "SI Appendix" in Sec. S1.C of the Supplemental Material [56], are nonlinear in all their arguments. Thus, Eq. (2) describes a constrained nonlinear optimization for which the FMINCON toolbox in MATLAB provides several well-developed and efficient numerical tools to find local minimizers. In other words, this optimization framework is "ready-made" for engineering design. For additional details on numerical aspects of this framework, see the flowchart in Fig. S3 and Sec. S2.E of the Supplemental Material [56].

All that remains now is to prescribe an objective function for the optimization. We are particularly interested in objective functions that can assess and optimize a variety of features of the stored elastic energy of the kirigami design. The challenge is that calculating an elastic energy based on high-fidelity modeling, such as finite-element-based or even bar-hinge-based modeling [57], is not efficient and thus creates a bottleneck in the optimization process. We instead develop an elastic model that can be implemented directly into MATLAB and evaluated using its fast solvers.

Our approach is formulated in detail in Sec. S2.A of the Supplemental Material [56] and illustrated in Fig. 2(e). We model the corner points of the kirigami pattern as

linear springs of zero rest length and unit stiffness and allow the panels to rotate and translate by a periodic motion that matches a bulk deformation expressed by the Bravais-lattice vectors $\boldsymbol{\ell}_1, \boldsymbol{\ell}_2$ in the figure. This deformation elongates the springs, generating an elastic energy expressed in terms of the panel rotations and translations and the Bravais-lattice vectors.

After minimizing out the translations and lattice vectors in Sec. S2.B of the Supplemental Material [56], we obtain the revealing form for the energy

$$E_{\text{spr}}(\eta_1, \eta_2, \eta_3, \eta_4) = \begin{bmatrix} \sum_{i=1,\dots,4} \mathbf{R}(\eta_i)\mathbf{s}_i \\ \sum_{i=1,\dots,4} \mathbf{R}(\eta_i)\mathbf{t}_i \\ \sum_{i=1,\dots,4} \mathbf{R}(\eta_i)\mathbf{u}_i \\ \sum_{i=1,\dots,4} \mathbf{R}(\eta_i)\mathbf{v}_i \end{bmatrix} \cdot \mathbf{G} \begin{bmatrix} \sum_{i=1,\dots,4} \mathbf{R}(\eta_i)\mathbf{s}_i \\ \sum_{i=1,\dots,4} \mathbf{R}(\eta_i)\mathbf{t}_i \\ \sum_{i=1,\dots,4} \mathbf{R}(\eta_i)\mathbf{u}_i \\ \sum_{i=1,\dots,4} \mathbf{R}(\eta_i)\mathbf{v}_i \end{bmatrix} \tag{3}$$

for an 8×8 symmetric and positive definite matrix $\mathbf{G}$ and the four panel rotations $\mathbf{R}(\eta_1), \dots, \mathbf{R}(\eta_4)$, as shown in the figure. The heuristics behind this energy are as follows. Prior to deformation, the four types of slits in the pattern satisfy $\sum_{i=1,\dots,4} \mathbf{s}_i = \mathbf{0}, \dots, \sum_{i=1,\dots,4} \mathbf{v}_i = \mathbf{0}$, because slits form closed loops. However, the deformed loops $\sum_{i=1,\dots,4} \mathbf{R}(\eta_i)\mathbf{s}_i, \dots, \sum_{i=1,\dots,4} \mathbf{R}(\eta_i)\mathbf{v}_i$ are typically broken ($\neq \mathbf{0}$) under the panel motions. Equation (3) employs these broken loops as the fundamental measures of elastic strain in the pattern. The matrix $\mathbf{G}$ in this formula quantifies how the slits influence each other elastically. Its components range between values 0 and 1 independent of the kirigami design and are reported in Eq. (S36) in Sec. S2.B of the Supplemental Material [56].

A final minimization allows us to quantify the elasticity of a bistable kirigami design in terms of a single kinematic variable:

$$E_{\text{act}}(\xi, \mathbf{s}_1, \mathbf{s}_2, \boldsymbol{\phi}) = \min_{\eta_3, \eta_4} \left\{ E_{\text{spr}}(0, \xi, \eta_3, \eta_4) \;\middle|\; \mathbf{s}_3, \mathbf{s}_4, \mathbf{t}, \mathbf{u}, \mathbf{v} \text{ solve Eq. (1)} \right\}. \tag{4}$$

We call this energy the *actuation energy*. It depends kinematically only on the angle ξ shown in Fig. 2(f), describing the relative rotation between the first and second panel of each unit cell as the overall pattern is actuated. It is non-negative and satisfies $E_{\text{act}} = 0$ when $\xi = 0$ and $\xi = \phi_2 - \phi_1$, reflecting the bistability hard encoded by Eq. (1).

This actuation energy integrates seamlessly with the optimization framework in Eq. (2), allowing us to efficiently explore and tune elastic properties of the kirigami design. In this work, we demonstrate this capability by optimizing the designs based on two properties of E_{act} through objective functions of the form

$$f_{\text{obj}}(\mathbf{s}_1, \mathbf{s}_2, \boldsymbol{\phi}) = \underbrace{c_b |E_b(\mathbf{s}_1, \mathbf{s}_2, \boldsymbol{\phi}) - E_b^{\text{targ}}|^2}_{\text{target energy barrier}} + \underbrace{c_1 |k_1(\mathbf{s}_1, \mathbf{s}_2, \boldsymbol{\phi}) - k_1^{\text{targ}}|^2}_{\text{target stiffness}}. \tag{5}$$

The first term tunes the designs so that the energy barrier between the designed stable states, $E_b(\mathbf{s}_1, \mathbf{s}_2, \boldsymbol{\phi}) = \max_{\xi \in (0, \phi_2 - \phi_1)} E_{\text{act}}(\xi, \mathbf{s}_1, \mathbf{s}_2, \boldsymbol{\phi})$, is driven toward a specified target $E_b^{\text{targ}} \geq 0$, reflecting the amount of work needed to actuate the pattern from one stable state to the other. The second term optimizes for the stiffness $k_1(\mathbf{s}_1, \mathbf{s}_2, \boldsymbol{\phi}) = \partial_\xi \partial_\xi E_{\text{act}}(0, \mathbf{s}_1, \mathbf{s}_2, \boldsymbol{\phi}) / (\lambda'(0))^2$ of the first stable state with respect to a *characteristic stretch* $\lambda(\xi) = \frac{|\mathbf{u}_1 - \mathbf{v}_1 + \mathbf{R}(\xi)(\mathbf{u}_2 - \mathbf{v}_2)|}{|\mathbf{u}_1 - \mathbf{v}_1 + \mathbf{u}_2 - \mathbf{v}_2|}$ that takes the value $\lambda(0) = 1$ in the first stable state and $\lambda(\phi_2 - \phi_1) = |\boldsymbol{\ell}_1^D| / |\boldsymbol{\ell}_1^R|$ in the second one (for more details, see Sec. S2.D of the Supplemental Material [56]). The designs are tuned by driving this stiffness toward a specified target $k_1^{\text{targ}} \geq 0$, allowing us to control whether we want this stable state to be "locked-in" or have some give at its typical performance loads. Design trade-offs are expected. For example, it is not usually possible to achieve a design that has both a high stiffness and a low overall energy barrier between the states. The numerical parameters $c_b, c_1 \geq 0$ express the desired importance of each term during an optimization. Though not done here, terms such as the maximum force and/or the stiffness of the second stable state can also be included in the objective function.

IV. REPRESENTATIVE EXAMPLE

We illustrate the optimization framework by tuning kirigami designs to achieve a variety of energy barriers under a prototypical square-to-rectangle transformation. In the optimization, the Bravais-lattice vectors are set at $\boldsymbol{\ell}_1^R = \mathbf{e}_1, \boldsymbol{\ell}_2^R = \mathbf{e}_2$ and $\boldsymbol{\ell}_1^D = 1.2\mathbf{e}_1, \boldsymbol{\ell}_2^D = 0.8\mathbf{e}_2$ to encode the effectively square and rectangular stable states and the moduli in Eq. (5) are taken as $c_b = 1$ and $c_1 = 0$ to focus on optimizing for a target energy barrier. In Figs. 3(a)–3(c), we show three optimized designs, obtained by prescribing the target energy barrier from left to right as $E_b^{\text{targ}} = 0.001, 0.0015, 0.003$ and performing the minimization in Eq. (2) in each case. A plot of the actuation energy $E_{\text{act}}(\xi)$ versus the stretch $\lambda(\xi)$ in Fig. 3(e) shows that each design achieves its target energy barrier. A randomly generated monostable design in Fig. 3(d) is included in Fig. 3(e) as another point of comparison.

To test the validity of the optimization framework, we fabricate a series of prototypes for all the aforementioned designs and examine their elastic energy and bistability experimentally. In comparing the theory to experiments, it

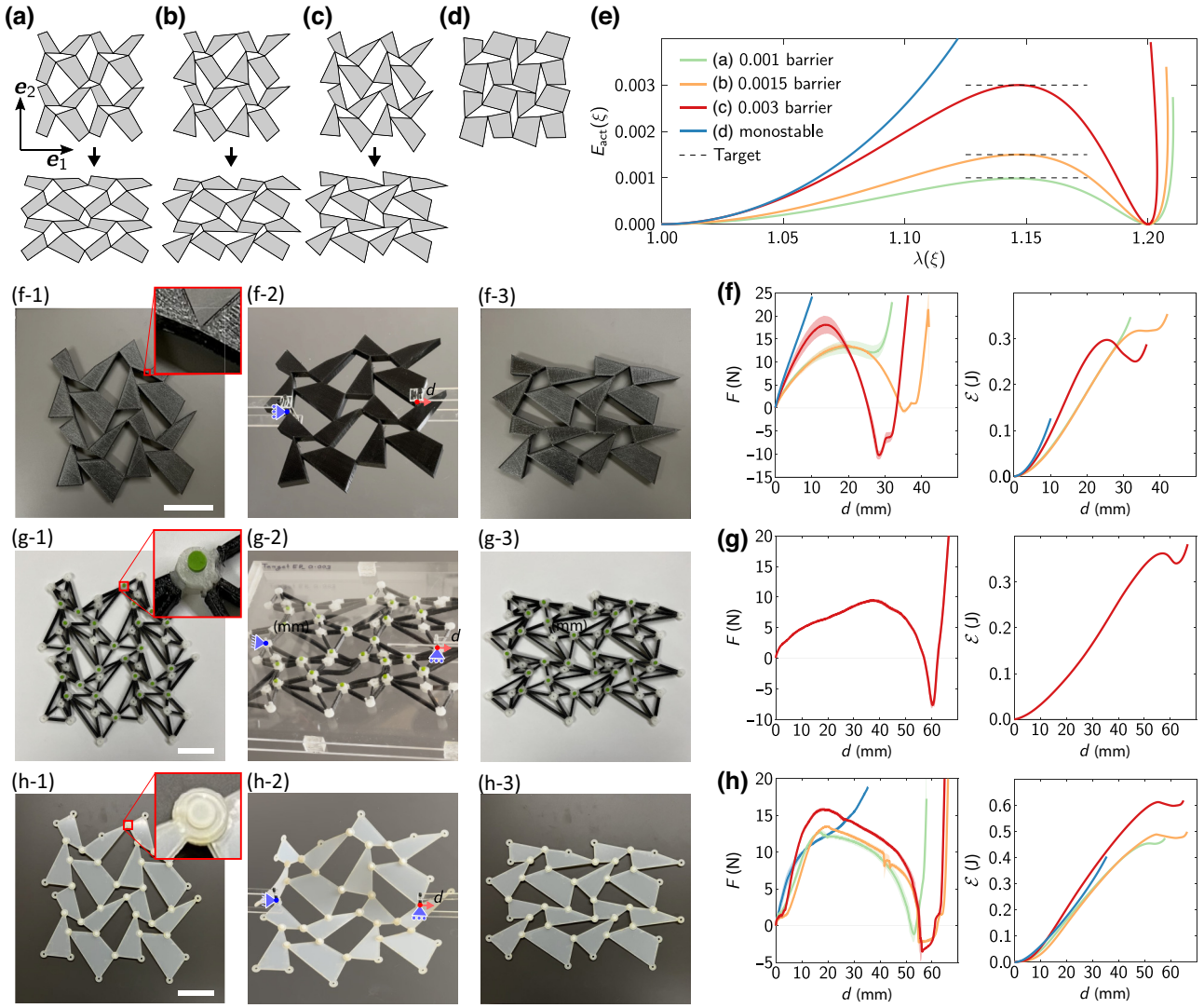

FIG. 3. A representative example and demonstration of bistability. (a)–(c) First and second stable states of the optimized patterns with energy barriers 0.001, 0.0015, and 0.003, respectively. Even though we represent them in 2×2 cell versions, these patterns are periodic. (d) The monostable geometry obtained by randomly perturbing the rotating-squares pattern. (e) The theoretical energy landscape of the patterns in (a)–(d), with horizontal lines indicating the target energy barriers; the legend shown here is valid throughout this figure. (f) Experimental results for a monolithic physical realization of the representative patterns, which involves compliant hinges; the solid lines are averages of three tensile tests and the shaded areas represent the standard deviation; the energy curves are obtained by numerically integrating the average force-displacement curves. (f-1, f-2, f-3) The first stable state, a snapshot of the deformation, and the second stable state, respectively, for a monolithic specimen with a 0.003 barrier. (g) The same as (f) but for a physical realization of the pattern involving skeletal bimaterial panels connected via perfect pins and capable of in-plane deformation via buckling of the internal beams. (h) The same as (f) but for a physical realization involving thin pin-jointed monomaterial panels that bend out of plane during deformation. Scale bar 5 cm.

is important to recognize that our mechanical model for the actuation energy is based on simplifying assumptions that enable us to efficiently optimize over the purely geometric parameters of the designs to achieve "some notion" of the target elastic properties. The goal is to provide design guidance in this large parameter space that gets trends right. Specifically, for a specified fabrication strategy, we expect that the energy barrier of the design in Fig. 3(a) is smaller than that of Fig. 3(b), which in turn is smaller than that of Fig. 3(c). We cannot, however, say much more than that: localized buckling, hinge elasticity, friction, viscoelasticity, and out-of-plane deformation, none of which are accounted for in our model, can influence the elastic behavior of these systems.

We propose three different fabrication strategies that differ in the way in which the energy barriers manifest as deformation, allowing us to explore the interplay between the fine design details inherent to prototyping and the

theoretical predictions of bistability. In all cases, the specimens are made of 2×2 unit cells and are tested in tension via a universal testing system using custom fixtures. In Figs. 3(f)–3(h), we show the raw force-displacement curves for tension tests of the fabricated samples, as well as their stored energy curves (obtained by integration of the force curves). The color scheme for the curves distinguishes the different designs, just as in Fig. 3(e). Additional details on the fabrication and experimental procedures, and on the dimensions of specimens, are given in Sects. S4 and S5 of the Supplemental Material [56]. We only report experimental results in the main text; Sec. S7 of the Supplemental Material [56] reports finite-element results that complement these findings.

In the first incarnation of our designs, we three-dimensionally (3D) print thick monolithic specimens made of "soft" thermoplastic polyurethane 95 (TPU 95), which represents the most conventional way to fabricate these metamaterials [15,40,45,58]. Notably, each sample exhibits negligible out-of-plane deformations due to its large thickness but also has elastic hinges that offer some resistance to the relative rotations between panels. In Fig. 3(f-1), we show the specimen with the largest (0.003) theoretical energy barrier in its first stable state; in Fig. 3(f-2), we show a snapshot of its in-plane deformation process during a tension test, with the distortions mostly concentrated in the hinge regions; and in Fig. 3(f-3), we show the second stable state, which is qualitatively similar to the theoretical one, while featuring some localized bending near the hinges. This case is clearly bistable—the force-displacement curve dips below zero, resulting in two clear energy minima. However, bistability is far from guaranteed, because hinge elasticity counteracts the geometric energy barriers that support a second stable state. In fact, the other two cases with the smaller theoretical energy barriers of 0.001 and 0.0015 are not bistable, as indicated by their force and energy curves.

Our second fabrication strategy eliminates the hinge elasticity that opposes bistability, while keeping the actuation essentially planar. To do this, we 3D print "skeletal" and bimaterial panels and assemble them via actual pin joints. The printed panels are composed of soft TPU bars and stiff nylon hinge regions to ensure that the deformations concentrate in the bars rather than in the neighborhood of the pin joints. We also place the specimens between clear acrylic plates during testing to prevent out-of-plane deformation. In Fig. 3(g-1), we show the 0.003 design fabricated in this fashion in its first stable state; in Fig. 3(g-2), we show an intermediate state during testing, illustrating how the deformation within the panels manifests as in-plane bending and buckling of the bars; and in Fig. 3(g-3), we show the second stable state, which now matches the theoretical one. The experimental force-displacement curves for this specimen clearly indicate bistability. Note that the presence of pin joints allows the specimen to be stress free in its second stable state even though the curve shows that the energy is nonzero in this state. We attribute the tilted energy curve to friction and material viscoelasticity, which dissipate energy during the tests. While this second incarnation is a better candidate to demonstrate bistability for a broad range of designs, fabrication has proved challenging and time consuming; for this reason, we only report results for the 0.003 specimen.

The final incarnation also features pin joints but the panels are now much thinner and laser cut out of polyethylene terephthalate glycol (PETG). As shown in Figs. 3(h-1)–3(h-3) for the 0.003 sample, these specimens transition between stable states via out-of-plane bending of the panels. The force and energy curves show that the patterns behave as expected—all the theoretically bistable designs are indeed bistable and the magnitudes of their energy barriers trend with that of the theory. In particular, the energy barrier for the 0.003 specimen is larger than the 0.0015 one, which is in turn larger than the 0.001 case. Here, significant frictional losses due to the panels pushing against each other and the rivets during out-of-plane deformation cause the energy curves to display nonzero values at the second equilibrium, even though these states are stress free.

Overall, these case studies validate our purely geometric design and optimization tools, as they showcase a variety of bistable metamaterials the shape change of which matches the theory and the energy barriers of which match the trends of the theory. We envision that the synergy between optimization and prototyping can be improved by introducing "nonuniversal" features into the objective function [Eq. (5)] that depend on the choice of fabrication strategy, although we do not pursue this further.

V. EXPLORING THE DESIGN AND OPTIMIZATION SPACE

We now highlight the richness of the design space by producing bistable kirigami patterns that exhibit a variety of axial and shearing shape changes. All examples correspond to reference lattice vectors $\overline{\boldsymbol{\ell}_1^R} = \mathbf{e}_1$ and $\overline{\boldsymbol{\ell}_2^R} = \mathbf{e}_2$ and achieve a second stable state given by one of two parametrizations of the deformed lattice vectors:

$$\begin{aligned} &\text{axial:} \quad \overline{\boldsymbol{\ell}_1^D} = \lambda_1 \mathbf{e}_1, \qquad \overline{\boldsymbol{\ell}_2^D} = \lambda_2 \mathbf{e}_2; \\ &\text{shear:} \quad \overline{\boldsymbol{\ell}_1^D} = \mathbf{e}_1 + \gamma \mathbf{e}_2, \quad \overline{\boldsymbol{\ell}_2^D} = \mathbf{e}_2 + \gamma \mathbf{e}_1. \end{aligned} \tag{6}$$

In Figs. 4(a)–4(e), we show designs obtained by optimizing the energy barrier using $c_b = 1, c_1 = 0$, and $E_b^{\text{targ}} = 0.003$ for a variety of $\lambda_{1,2}$ and γ.

In Fig, 4(a) in particular, we showcase a suite of designs corresponding to axial shape morphing with λ_1 and λ_2 varied uniformly from 0.8 (contraction) to 1.3 (expansion) in a design matrix. The coloring scheme reflects whether the optimized design achieves the target 0.003 energy barrier.

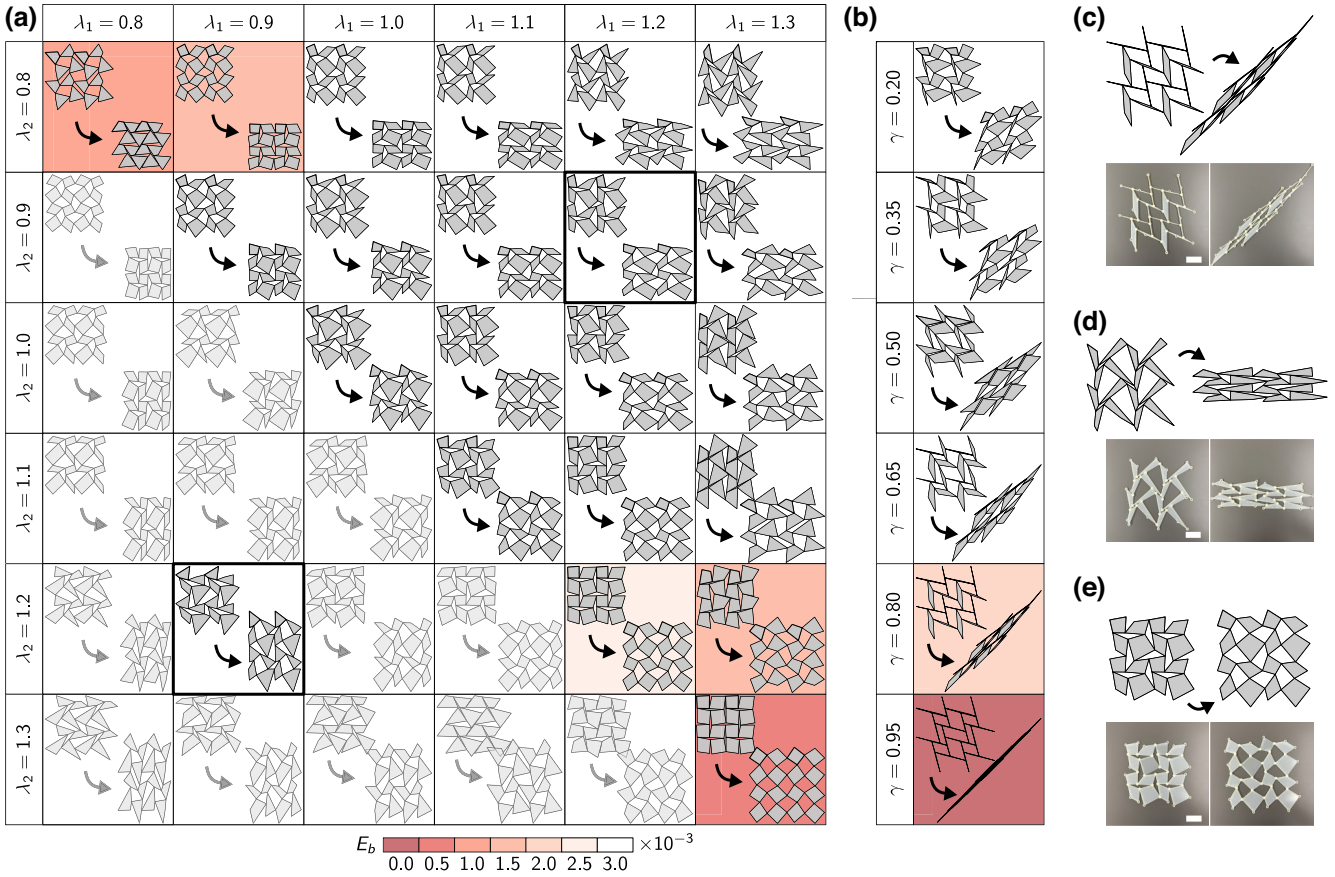

FIG. 4. Design explorations. (a) A matrix of designs optimized to attain axial shape transformation (from a square to another square or rectangle) of varying degree, with a target energy barrier of 0.003. The designs are color coded according to the actual value of the barrier achieved during optimization, as indicated in the legend below (b). Shaded designs in the lower diagonal are simply rotations of the corresponding designs in the upper diagonal. (b) The suite of designs that undergo a shear-type shape transformation. λ_1, λ_2, and γ, which control the magnitude of the shape change, are defined in Eq. (6). (c)–(e) The first and second stable states of various patterns, with their monomaterial physical realizations: (c) the pattern designed to undergo extreme shear-type morphing, with $\gamma = 0.8$; (d) extreme nonauxetic morphing; (e) extreme auxetic morphing. In all of the experimental images, scale bar 5 cm.

As the coloring indicates, the richness of the design space depends significantly on the shape morphing. Nonauxetic designs where one side contracts and the other expands appear to be much more amenable to the large energy barriers than auxetic ones. In fact, the most extreme auxetic design—the purely dilation one in the lower-right corner of the figure—is only a slight modification of the purely mechanistic rotating-squares pattern, even though we optimize for a high energy barrier. This observation suggests that the rotating-squares pattern is perhaps the singular template for extreme dilation in quad kirigami. Another interesting point concerns symmetry and nonuniqueness. As illustrated in the design matrix, every optimized design in the upper-right quadrant, $(\lambda_1, \lambda_2) = (x, y)$, is related to one in the lower left, $(\lambda_1, \lambda_2) = (y, x)$, by a 90° rotation. These rotated designs are shaded in Fig. 4(a). In some of the less extreme cases, however, more than one design achieves the target energy and shape change. We illustrate this point by highlighting a $(\lambda_1, \lambda_2) = (0.9, 1.2)$ optimized design that is distinct from the $(\lambda_1, \lambda_2) = (1.2, 0.9)$ case shown.

In Fig. 4(b), we also showcase a suite of designs, this time for the shear case in Eq. (6), with γ evolving uniformly from 0.2 to 0.95. Again the design space shrinks as the shear becomes more extreme, making it harder for the optimized design to achieve the target energy barrier $E_b^{\text{targ}} = 0.003$. Note that the maximum shear in this setting is $\gamma_{\max} = 1$, since this shape change takes an effectively square reference domain to a line. Evolving the shear monotonically to this maximum leads to panels that degenerate to lines and slits to parallelograms. A curious yet persistent observation in Figs. 4(a) and 4(b) (and in Sec. S2.F of the Supplemental Material [56]) is that extremal shape change seems always to correspond to designs with parallelogram slits, i.e., designs known to always possess a single-degree-of-freedom (DOF) mechanism [53]. Whether this observation suggests a universal relationship between mechanism-based designs and

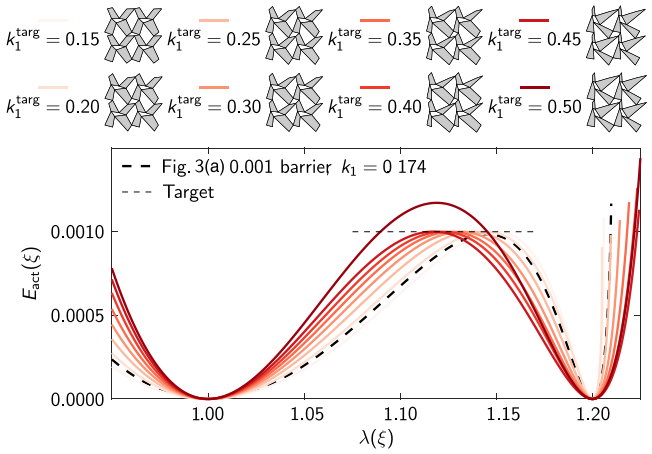

FIG. 5. Additional design explorations. Theoretical energy landscapes of patterns designed to display various target stiffness k_1^{targ}, while maintaining a barrier around 0.001. In the legend, we show the first stable states of all such patterns.

bistable ones remains to be seen but it is nonetheless compelling evidence of some sort of connection.

Returning to prototyping, In Figs. 4(c)–4(e), we highlight the design and fabrication of three examples of extreme shape change: a shear case, a nonauxetic case, and an auxetic purely dilational case. In all cases, we employ the third fabrication strategy discussed above, with pin joints and laser-cut PETG panels, since specimens made in this way are easy to produce and exhibit a "clean" performance. As shown in the figure, each sample is bistable and displays the predicted shape change. The supplementary videos listed and described in Sec. S6 of the Supplemental Material [56] provide further illustrations of the bistability of these samples.

We end this section by showcasing designs tuned to achieve multiple objectives at the same time. Going back to the prototypical square-to-rectangular transformation studied previously, in Fig. 5 we show designs that have been optimized for both a target energy barrier and a target stiffness in its first stable state. Specifically, we fix $c_b = 1$, $c_1 = 0.002$ and $E_b^{\text{targ}} = 0.001$ and vary the target stiffness uniformly from $k_1^{\text{targ}} = 0.15$ to 0.50 to produce eight optimized designs. As the plot indicates, we have control of both the stiffness and the energy barrier over a wide range of the parameter space (from $k_1^{\text{targ}} = 0.1$ to 0.45). However, once k_1^{targ} is sufficiently large, the energy barrier can no longer be held fixed. Instead it tilts up, reflecting a trade-off between high stiffness and low energy.

VI. HETEROGENEOUS SHAPE CHANGE

We now go beyond periodic structures and show how our design and optimization methods can be integrated into a simple recipe to program bistable kirigami metamaterials with target heterogeneous shapes. We explain the approach through the square-to-bowtie transformation shown in Figs. 6(a)–6(c), before illustrating its versatility through the complex examples in Figs. 6(d) and 6(e).

In the transformation in Fig. 6(a), the quad cells of the square mesh are mapped one to one to the cells of the bowtie mesh through the lattice transformations $\boldsymbol{\ell}_1^R(i,j) \mapsto \boldsymbol{\ell}_1^D(i,j)$ and $\boldsymbol{\ell}_2^R(i,j) \mapsto \boldsymbol{\ell}_2^D(i,j)$, indexed by (i,j) as shown. While the bowtie mesh is not homogeneous, its lattice vectors vary slowly from cell to cell to produce the overall shape. We exploit these slow variations, and the key fact that the lattice vectors are designer inputs for bistability in Eq. (1), to obtain a kirigami pattern capable of transforming from the square to the bowtie shape at very little stress.

The general idea is as follows (for more details, see Sec. S3 of the Supplemental Material [56]). After an initialization step to seed the design of a single kirigami cell, we produce a global kirigami pattern through a marching procedure that is fundamentally local. At each (i,j), indicating corresponding quads in the two meshes, we prescribe the lattice vectors for a bistable design in Eq. (1) as $\boldsymbol{\ell} = \boldsymbol{\ell}(i,j)$. Next, we choose the remaining DOFs in this equation as a set of minimizers $\mathbf{s}_1 = \mathbf{s}_1(i,j), \mathbf{s}_2 = \mathbf{s}_2(i,j), \boldsymbol{\phi} = \boldsymbol{\phi}(i,j)$ to Eq. (2), with

$$f_{\text{obj}}(\mathbf{s}_1, \mathbf{s}_2, \boldsymbol{\phi}) = \left|(\mathbf{s}_1, \mathbf{s}_2, \boldsymbol{\phi}) - (\mathbf{s}_1^{\text{prev}}, \mathbf{s}_2^{\text{prev}}, \boldsymbol{\phi}^{\text{prev}})\right|^2, \quad (7)$$

where $(\mathbf{s}_1^{\text{prev}}, \mathbf{s}_2^{\text{prev}}, \boldsymbol{\phi}^{\text{prev}})$ is from a previously computed neighboring cell. Finally, we choose $\mathbf{s}_3 = \mathbf{s}_3(i,j), \ldots, \mathbf{v} = \mathbf{v}(i,j)$ to solve Eq. (1) for the above (i,j) design variables. This recipe furnishes a bistable kirigami cell that takes the shape of the two (i,j) quads as its stable states. Iterating on it produces two global patterns, one with the desired overall square shape and another with the desired bowtie. However, each has small gaps between neighboring unit cells due to the spatial variations of the lattice vectors (see Fig. S5 in the Supplemental Material [56]). A final averaging step glues each pattern together and furnishes the kirigami designs for the two shapes shown in Fig. 6(b).

The averaging part of the design procedure yields panels in the bowtie that are distorted slightly from their counterparts in the square pattern, meaning that the transformation is not stress free. To verify bistability, we supplement the procedure with a truss-based model of the pattern under load in Fig. 6(c), based on the bar-hinge model of Ref. [57]. The model assumes that the square pattern is the stress-free reference configuration, that bars deform only axially, and that their material is linear elastic (see Sec. S7.D of the Supplemental Material [56]). The pattern is then supported by rollers on its left boundary and loaded by a uniform set of horizontal nodal forces F on its right [Fig. 6(c-1)]. The overall horizontal displacement, denoted d, increases smoothly under force control until the configuration in Fig. 6(c-2), where it jumps from $d/|\boldsymbol{\ell}_1^R| \approx 1$ to $d/|\boldsymbol{\ell}_1^R| \approx 1.6$ on a further increase of load. Unloading

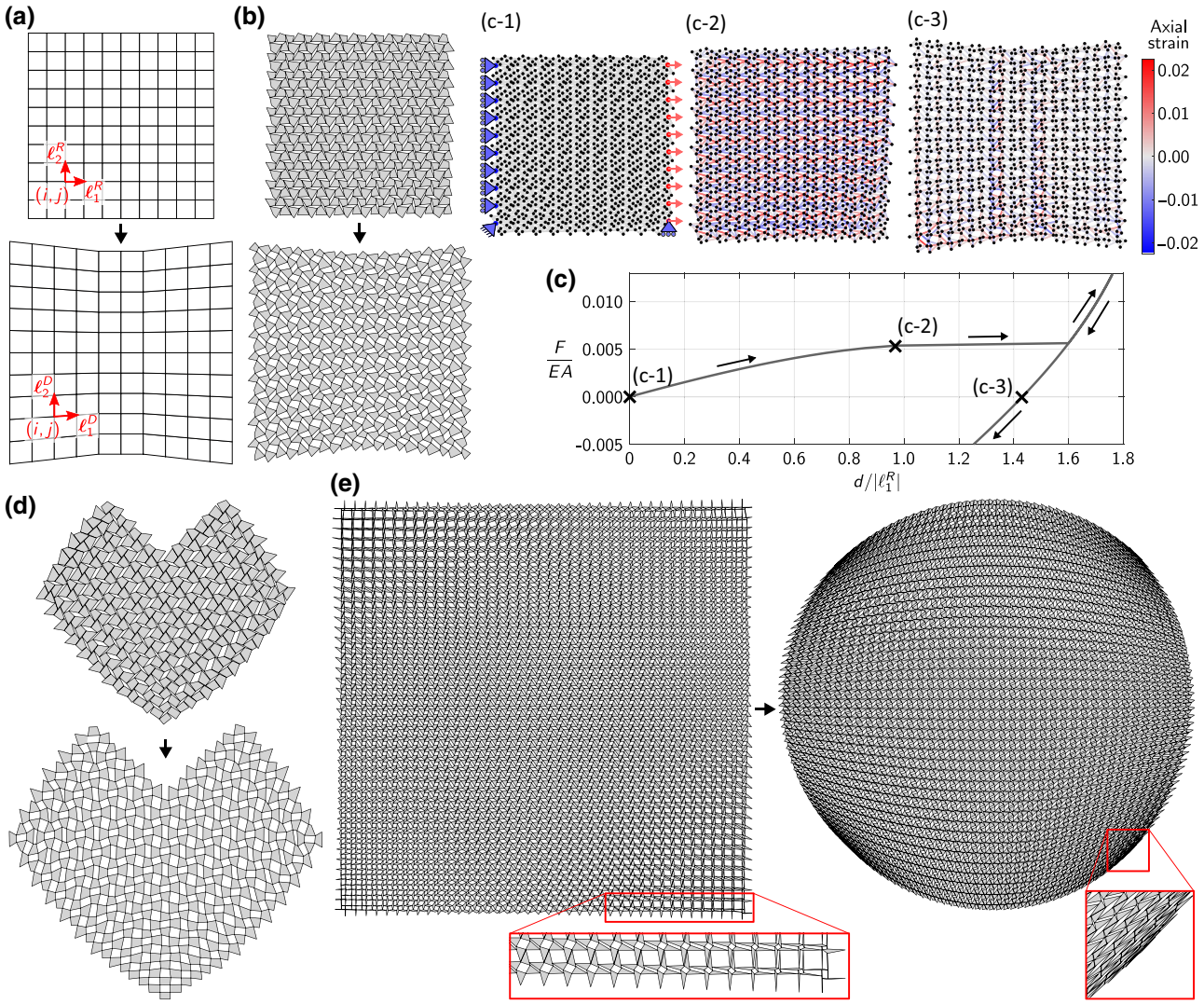

FIG. 6. Heterogeneous designs for complex shape change. (a)–(c) An example of a pattern designed to morph from a square to a bowtie shape: (a) the mesh grids of the two desired stable states, which give information on the lattice vectors to be prescribed to each unit cell; (b) the optimized pattern in its first and second stable states; (c) the numerical validation of bistability via a geometrically nonlinear truss model, showing a force-displacement curve, with arrows indicating the direction of loading or unloading and three snapshots of the deformation. Inset (c-1) indicates the boundary conditions for the simulation. (d) The beating-heart pattern, in its first and second stable states. (e) A structure designed to morph from a square to a disk, in its first and second stable states.

after the jump, the curve crosses the zero-force axis away from the origin, providing a demonstration of bistability. The bowtie shape of Fig. 6(c-3), showing small residual strains, is the second equilibrium configuration.

The key point is not that we have identified a square-to-bowtie bistable design; it is that the procedure is exceedingly simple and general. It only relies on the fact that we have a one-to-one "regular" quad mesh of the two stable states with lattice vectors that vary slowly from quad to quad (regular means that the meshes can be mapped bijectively to a connected subset of the $\mathbb{Z}^2$ lattice). Such meshes are easy to obtain for a wide variety of shapes, so our procedure can be employed for a myriad of target bistable patterns. In Figs. 6(d) and 6(e), we illustrate two such examples, a "beating-heart" and a square-to-disk transformation.

For the heart, we mesh the compact state (see Fig. S7A in the Supplemental Material [56]) using the "Quasi-Structured Quad" setting from the freely available software GMSH [59] and dilate this mesh to obtain the enlarged meshed state. The design procedure iterates through the cells in these meshes to produce the kirigami pattern. We have studied a variety of dilation factors $\lambda \geq 1$. Increasing this factor monotonically leads to a compact state where the slits degenerate to lines (closed slits) and a dilated state where the slits tend toward being fully open. At sufficiently

large values of λ, the panels begin to overlap in the compact state, violating the inequality constraints in Eq. (2). In Fig. 6(d), we show a $\lambda = 1.25$ design obtained by our methods. This level of dilation is actually quite impressive given the heterogeneity of the cells and certain basic limitations of quad kirigami. The rotating-squares pattern, for instance, transforms from its fully closed to fully open state by a uniform dilation of $\lambda_{rs} = \sqrt{2} \approx 1.41$, which likely sets the theoretical upper bound on dilation for these types of patterns.

Our last demonstration of heterogeneous morphing in Fig. 6(e) showcases a square-to-disk kirigami pattern. The quad-mesh precursors are obtained by discretizing the square domain uniformly on $(-1,1)^2$ using a 40×40 set of square cells and then deforming this mesh smoothly to the unit disk by the elliptical-grid mapping $(x,y) \mapsto (x\sqrt{1-y^2/2}, y\sqrt{1-x^2/2})$. This mapping spreads the mesh distortions smoothly from the interior to four singular points, corresponding to the deformed corners of the square (see Fig. S7B in the Supplemental Material [56]). The design procedure accounts for this spreading by producing cells in the square the slit area of which increases dramatically from its center to its corners; the dichotomy is reversed in the disk state. As shown in Fig. 6(e), the corners of the square essentially collapse inward, closing their slits, to achieve the disk as the second stable state. A key ingredient to the impressive display of shape change in this example is the scalability of our methods. Since the design procedure is completely local, we can produce kirigami designs with target shapes that involve thousands of unit cells in a matter of minutes on a standard laptop.

VII. CONCLUSIONS

In summary, we have introduced a set of principles to rationally design and optimize bistable planar kirigami metamaterials, starting from a well-known nonbistable template. Importantly, the optmization tools incorporate a reduced-order elastic model, enabling on-demand design guidance for bistable kirigami with a rich variety of shape-morphing capabilities and energy landscapes—it provides experimentalists access to new designs in a matter of minutes. Optimized bistable designs are exemplified through a variety of fabrication strategies, with experimental results that largely match the shape change of the theory and the trends in the target elastic properties. Open questions remain. The fine details of fabrication introduce features not present in the current design framework, e.g., hinge elasticity, beam buckling, and panel bending. One challenge is to adapt the framework to account for these details, while ensuring that it still remains an efficient design tool. Another avenue concerns generality. The basic ingredients of our framework are geometric perturbations of a unit cell and intercell compatibility constraints. As these ingredients are found across metamaterial templates, design formulas that hard encode bistability, such as Eq. (1), are perhaps ripe for discovery in a wide range of metamaterials.

ACKNOWLEDGMENTS

P.P. and Y.P. acknowledge support from the National Science Foundation (NSF) (Grant No. CMMI-CAREER-2237243) and from the Army Research Office (Grant No. ARO-W911NF2310137). P.C. and I.N. acknowledge support from the NSF (Grant No. CMMI-2045191). P.C. and I.N. thank Damiano Pasini and Christelle Combescure for constructive suggestions.

[1] P. M. Reis, A perspective on the revival of structural (in)stability with novel opportunities for function: From buckliphobia to buckliphilia, J. Appl. Mech. **82**, 111001 (2015).
[2] N. Hu and R. Burgueño, Buckling-induced smart applications: Recent advances and trends, Smart Mater. Struct. **24**, 063001 (2015).
[3] D. M. Kochmann and K. Bertoldi, Exploiting microstructural instabilities in solids and structures: From metamaterials to structural transitions, Appl. Mech. Rev. **69**, 050801 (2017).
[4] Y. Forterre, J. M. Skotheim, J. Dumais, and L. Mahadevan, How the Venus flytrap snaps, Nature **433**, 421 (2005).
[5] J. A. Faber, A. F. Arrieta, and A. R. Studart, Bioinspired spring origami, Science **359**, 1386 (2018).
[6] S. Pellegrino, in *Deployable Structures* (Springer Vienna, 2001), p. 1, https://link.springer.com/book/10.1007/978-3-7091-2584-7#bibliographic-information.
[7] T. Chen, O. R. Bilal, K. Shea, and C. Daraio, Harnessing bistability for directional propulsion of soft, untethered robots, Proc. Natl. Acad. Sci. **115**, 5698 (2018).
[8] Y. Tang, Y. Chi, J. Sun, T. H. Huang, O. H. Maghsoudi, A. Spence, J. Zhao, H. Su, and J. Yin, Leveraging elastic instabilities for amplified performance: Spine-inspired high-speed and high-force soft robots, Sci. Adv. **6**, eaaz6912 (2020).
[9] Y. Chi, Y. Li, Y. Zhao, Y. Hong, Y. Tang, and J. Yin, Bistable and multistable actuators for soft robots: Structures, materials, and functionalities, Adv. Mater. **34**, 2110384 (2022).
[10] M. T. A. Saif, On a tunable bistable MEMS-theory and experiment, J. Microelectromech. Syst. **9**, 157 (2000).
[11] Y. Cao, M. Derakhshani, Y. Fang, G. Huang, and C. Cao, Bistable structures for advanced functional systems, Adv. Funct. Mater. **31**, 2106231 (2021).
[12] D. R. Lapp, Exploring "extreme" physics with an inexpensive plastic toy popper, Phys. Ed. **43**, 492 (2008).
[13] A. Pandey, D. E. Moulton, D. Vella, and D. P. Holmes, Dynamics of snapping beams and jumping poppers, Europhys. Lett. **105**, 24001 (2014).
[14] M. Vangbo, An analytical analysis of a compressed bistable buckled beam, Sens. Actuators A: Phys. **69**, 212 (1998).

[15] A. Rafsanjani and D. Pasini, Bistable auxetic mechanical metamaterials inspired by ancient geometric motifs, Extreme Mech. Lett. **9**, 291 (2016).
[16] K. Iqbal and S. Pellegrino, in *41st Structures, Structural Dynamics, and Materials Conference and Exhibit* (American Institute for Aeronautics and Astronautics, Atlanta, GA, U.S.A., 2000), p. 1385.
[17] Z. Chen, Q. Guo, C. Majidi, W. Chen, D. J. Srolovitz, and M. P. Haataja, Nonlinear geometric effects in mechanical bistable morphing structures, Phys. Rev. Lett. **109**, 114302 (2012).
[18] Y. Li and J. Yin, Metamorphosis of three-dimensional kirigami-inspired reconfigurable and reprogrammable architected matter, Mater. Today Phys. **21**, 100511 (2021).
[19] X. Zhang, J. Ma, M. Li, Z. You, X. Wang, Y. Luo, K. Ma, and Y. Chen, Kirigami-based metastructures with programmable multistability, Proc. Natl. Acad. Sci. **119**, e2117649119 (2022).
[20] J. L. Silverberg, A. A. Evans, L. McLeod, R. C. Hayward, T. Hull, C. D. Santangelo, and I. Cohen, Using origami design principles to fold reprogrammable mechanical metamaterials, Science **345**, 647 (2014).
[21] B. H. Hanna, J. M. Lund, R. J. Lang, S. P. Magleby, and L. L. Howell, Waterbomb base: A symmetric single-vertex bistable origami mechanism, Smart Mater. Struct. **23**, 094009 (2014).
[22] R. von Mises, Über die stabilitätsprobleme der elastizitätstheorie, ZAMM—J. Appl. Math. Mech./Z. Angew. Math. Mech. **3**, 406 (1923).
[23] B. Haghpanah, L. Salari-Sharif, P. Pourrajab, J. Hopkins, and L. Valdevit, Multistable shape-reconfigurable architected materials, Adv. Mater. **28**, 7915 (2016).
[24] K. A. Seffen, Mechanical memory metal: A novel material for developing morphing engineering structures, Scr. Mater. **55**, 411 (2006).
[25] T. Schioler and S. Pellegrino, Space frames with multiple stable configurations, AIAA J. **45**, 1740 (2007).
[26] G. Chen, Y. Gou, and A. Zhang, Synthesis of compliant multistable mechanisms through use of a single bistable mechanism, J. Mech. Des. **133**, 081007 (2011).
[27] S. Shan, S. H. Kang, J. R. Raney, P. Wang, L. Fang, F. Candido, J. A. Lewis, and K. Bertoldi, Multistable architected materials for trapping elastic strain energy, Adv. Mater. **27**, 4296 (2015).
[28] D. Restrepo, N. D. Mankame, and P. D. Zavattieri, Phase transforming cellular materials, Extreme Mech. Lett. **4**, 52 (2015).
[29] A. Ion, L. Wall, R. Kovacs, and P. Baudisch, in *Proceedings of the 2017 CHI Conference on Human Factors in Computing Systems*, CHI '17 (Association for Computing Machinery, New York, 2017), p. 977.
[30] T. Chen, J. Mueller, and K. Shea, Integrated design and simulation of tunable, multi-state structures fabricated monolithically with multi-material 3D printing, Sci. Rep. **7**, 45671 (2017).
[31] S. Liu, A. I. Azad, and R. Burgueño, Architected materials for tailorable shear behavior with energy dissipation, Extreme Mech. Lett. **28**, 1 (2019).
[32] J. L. Silverberg, J. Na, A. A. Evans, B. Liu, T. C. Hull, C. D. Santangelo, R. J. Lang, R. C. Hayward, and I. Cohen, Origami structures with a critical transition to bistability arising from hidden degrees of freedom, Nat. Mater. **14**, 389 (2015).
[33] C. Jianguo, D. Xiaowei, Z. Ya, F. Jian, and T. Yongming, Bistable behavior of the cylindrical origami structure with Kresling pattern, J. Mech. Des. **137**, 061406 (2015).
[34] K. Kuribayashi, K. Tsuchiya, Z. You, D. Tomus, M. Umemoto, T. Ito, and M. Sasaki, Self-deployable origami stent grafts as a biomedical application of Ni-rich TiNi shape memory alloy foil, Mater. Sci. Eng.: A **419**, 131 (2006).
[35] F. Feng, P. Plucinsky, and R. D. James, Helical Miura origami, Phys. Rev. E **101**, 033002 (2020).
[36] E. T. Filipov and M. Redoutey, Mechanical characteristics of the bistable origami hypar, Extreme Mech. Lett. **25**, 16 (2018).
[37] R. J. Lang, S. Magleby, and L. Howell, Single degree-of-freedom rigidly foldable cut origami flashers, J. Mech. Robot. **8**, 031005 (2016).
[38] M. Arya, D. Webb, S. C. Bradford, L. Adams, V. Cormarkovic, G. Wang, M. Mobrem, K. Neff, N. Beidleman, J. D. Stienmier, G. Freebury, K. A. Medina, D. Hepper, D. E. Turse, G. Antoun, C. Rupp, and L. Hoffman, in *AIAA Scitech 2021 Forum* (American Institute for Aeronautics and Astronautics, 2021), p. 0904.
[39] J. N. Grima and K. E. Evans, Auxetic behavior from rotating squares, J. Mater. Sci. Lett. **19**, 1563 (2000).
[40] Y. Tang and J. Yin, Design of cut unit geometry in hierarchical kirigami-based auxetic metamaterials for high stretchability and compressibility, Extreme Mech. Lett. **12**, 77 (2017).
[41] S. Pellegrino and C. R. Calladine, Matrix analysis of statically and kinematically indeterminate frameworks, Int. J. Solids Struct. **22**, 409 (1986).
[42] T. C. Lubensky, C. L. Kane, X. Mao, A. Souslov, and K. Sun, Phonons and elasticity in critically coordinated lattices, Rep. Prog. Phys. **78**, 073901 (2015).
[43] N. Singh and M. van Hecke, Design of pseudo-mechanisms and multistable units for mechanical metamaterials, Phys. Rev. Lett. **126**, 248002 (2021).
[44] B. Deng, A. Zareei, X. Ding, J. C. Weaver, C. H. Rycroft, and K. Bertoldi, Inverse design of mechanical metamaterials with target nonlinear response via a neural accelerated evolution strategy, Adv. Mater. **34**, 2206238 (2022).
[45] G. P. T. Choi, L. H. Dudte, and L. Mahadevan, Programming shape using kirigami tessellations, Nat. Mater. **18**, 999 (2019).
[46] L. H. Dudte, E. Vouga, T. Tachi, and L. Mahadevan, Programming curvature using origami tessellations, Nat. Mater. **15**, 583 (2016).
[47] F. Feng, X. Dang, R. D. James, and P. Plucinsky, The designs and deformations of rigidly and flat-foldable quadrilateral mesh origami, J. Mech. Phys. Solids **142**, 104018 (2020).
[48] X. Dang, F. Feng, P. Plucinsky, R. D. James, H. Duan, and J. Wang, Inverse design of deployable origami structures that approximate a general surface, Int. J. Solids Struct. **234**, 111224 (2022).
[49] L. H. Dudte, G. P. T. Choi, and L. Mahadevan, An additive algorithm for origami design, Proc. Natl. Acad. Sci. **118**, e2019241118 (2021).

[50] A. Walker and T. Stankovic, Algorithmic design of origami mechanisms and tessellations, Commun. Mater. **3**, 4 (2022).
[51] L. H. Dudte, G. P. Choi, K. P. Becker, and L. Mahadevan, An additive framework for kirigami design, Nat. Comput. Sci. **3**, 443 (2023).
[52] G. P. T. Choi, L. H. Dudte, and L. Mahadevan, Compact reconfigurable kirigami, Phys. Rev. Res. **3**, 043030 (2021).
[53] Y. Zheng, I. Niloy, P. Celli, I. Tobasco, and P. Plucinsky, Continuum field theory for the deformations of planar kirigami, Phys. Rev. Lett. **128**, 208003 (2022).
[54] A. Rafsanjani and K. Bertoldi, Buckling-induced kirigami, Phys. Rev. Lett. **118**, 084301 (2017).
[55] Y. Yang, M. A. Dias, and D. P. Holmes, Multistable kirigami for tunable architected materials, Phys. Rev. Mater. **2**, 110601 (2018).
[56] See the Supplemental Material http://link.aps.org/supplemental/10.1103/PhysRevApplied.22.014073 for further details on theoretical derivations, the optimization framework, fabrication and experimental procedures, and numerical simulations.
[57] K. Liu and G. H. Paulino, Nonlinear mechanics of non-rigid origami: An efficient computational approach, Proc. R. Soc. A: Math., Phys. Eng. Sci. **473**, 20170348 (2017).
[58] L. Wu and D. Pasini, In situ activation of snap-through instability in multi-response metamaterials through multistable topological transformation, Adv. Mater. **35**, 2301109 (2023).
[59] C. Geuzaine and J.-F. Remacle, GMSH: A 3-D finite element mesh generator with built-in pre-and post-processing facilities, Int. J. Numer. Methods Eng. **79**, 1309 (2009).